

V61

## He-Ne Laser

Fritz Ali Agildere  
fritz.agildere@udo.edu

Jan Lucca Viola  
janlucca.viola@udo.edu

Experiment: November 25, 2024

Submission: December 3, 2024

TU Dortmund – Department of Physics

# Contents

<b>1</b>	<b>Objective</b>	<b>1</b>
<b>2</b>	<b>Background</b>	<b>1</b>
2.1	Components of a laser	1
2.2	Processes in the active medium	2
2.3	Necessity of multiple levels	4
2.4	Stability for different resonators	6
2.5	Transverse and longitudinal modes	8
2.6	Doppler broadening of the transition	9
2.7	Brewster window and polarization	10
<b>3</b>	<b>Procedure</b>	<b>11</b>
3.1	Aligning the Laser	11
3.2	Verifying the Stability Condition	11
3.3	Observing Transverse Modes	11
3.4	Determining the Polarization	12
3.5	Analyzing Spectra in Multimode Operation	12
3.6	Measuring the Wavelength	12
<b>4</b>	<b>Results</b>	<b>12</b>
4.1	Verifying the Stability Condition	12
4.2	Observing Transverse Modes	13
4.2.1	TEM <sub>00</sub>	13
4.2.2	TEM <sub>10</sub>	15
4.2.3	TEM <sub>20</sub>	16
4.3	Determining the Polarization	16
4.4	Analyzing Spectra in Multimode Operation	17
4.5	Measuring the Wavelength	20
<b>5</b>	<b>Discussion</b>	<b>20</b>
	<b>References</b>	<b>21</b>

# 1 Objective

To understand the characteristics of a He-Ne laser, several different configurations are adjusted and their radiation properties measured. This includes the wavelength, intensity distribution, polarization, mode spectrum, as well as the influence of mirror type and resonator length.

## 2 Background [1]

Lasers are ubiquitous tools of modern physics due to their useful properties, characterized by the emission of coherent light with narrow spectral linewidth, low divergence and high power density. They are named after the acronym for light amplification by stimulated emission of radiation, describing the fundamental mechanism for the production of laser radiation. This will be explored in the following, both in the general as well as the special case of the He-Ne laser.

### 2.1 Components of a laser

The basic setup of a typical laser consists of three main components, namely an active medium, a pumping mechanism and the resonator cavity.

Inside the active medium, realized using materials such as semiconductors or gas mixtures, photons are emitted from atomic transitions to energetically lower states. The energy difference  $\Delta E$  between the involved electron levels is therefore the main determinant of wavelength  $\lambda$  and frequency  $f$  via  $\Delta E = hf$ .

To excite electrons in the active medium to higher levels, an energy source is required. This is the role of the pumping mechanism, which can be implemented using electrons or photons. The latter case is called optical pumping, as another separate light source tuned to the respective  $\Delta E$  value is used to induce transitions to excited states.

Amplification of the emitted radiation is achieved in the active medium. Instead of using superradiant lasers, which have high gain factors and divergence, or impractically long constructions, mirrors can be used to create a resonator cavity. The resulting standing waves correspond to multiple passes through the material and can generate a stable beam with low divergence, which can exit through a semitransparent window. The mirror geometry can be adapted to the desired function with flat or concave designs.

## 2.2 Processes in the active medium

There are three main processes shown in Figure 1 occurring inside the active medium to facilitate the operation of a laser.



**Figure 1:** Schematic depiction of relevant processes inside the active medium. [1]

Raising the energy of an electron by  $\Delta E = E_2 - E_1$  requires the annihilation of an incident photon that fulfills the condition

$$\Delta E = hf_{12} ,$$

where  $h$  is the Planck constant. This process is referred to as absorption. The number of transitions per time and volume is proportional to the density of ground state electrons  $N_1$  as well as the photon flux or number per area and time  $\varphi$  via

$$\left. \frac{dN_1}{dt} \right|_{\text{ab}} = -\sigma_{12} N_1 \varphi ,$$

with  $\sigma_{12}$  denoting the effective cross section for absorbing a photon. From this also follows the typical exponential intensity reduction

$$\left. \frac{dI}{dx} \right|_{\text{ab}} = -\sigma_{12} N_1 I ,$$

where  $\alpha = -\sigma_{12} N_1$  gives the absorption coefficient.

When an atom is in an excited state, it returns to the ground state after a time interval, the duration of which follows some random distribution with mean lifetime  $\tau$ . Due to its stochastic nature, this process is called spontaneous emission and has no predefined direction or phase. The density in the higher level then follows

$$\left. \frac{dN_2}{dt} \right|_{\text{sp}} = -\tau^{-1} N_2 .$$

Besides this, emission can also be initiated by an incoming photon of appropriate frequency. This is called stimulated emission and results in the production of radiation with the same energy, direction and phase as the inducing quantum. As the inverse process to absorption,

$$\left. \frac{dN_2}{dt} \right|_{\text{st}} = -\sigma_{21} N_2 \varphi ,$$

describes the time derivative and

$$\left. \frac{dI}{dx} \right|_{\text{st}} = \sigma_{21} N_2 I ,$$

the corresponding intensity relation. This means that stimulated emission leads to an increase in intensity, serving as a potential mechanism for amplification when there are more electrons in the excited state than in the ground state and losses are compensated for. This phenomenon is referred to as population inversion.

The cross sections can be identified with the Einstein coefficients  $B_{ij}$  via

$$\sigma_{ij} = B_{ij} h f_{ij} / c ,$$

where  $c$  is the speed of light in vacuo. Furthermore, for emission and absorption, the thermodynamic or quantum mechanical relation

$$g_1 \sigma_{12} = g_2 \sigma_{21}$$

holds, with  $g_1$  and  $g_2$  defining the degrees of degeneracy for the ground and excited states. Hereafter, it is assumed that  $E_1$  and  $E_2$  have the same number of sublevels, so  $g_1 = g_2$  for  $\sigma_{12} = \sigma_{21}$  and

$$B \equiv B_{12} = B_{21} .$$

The reciprocal decay timescale defines another Einstein coefficient

$$A = \tau^{-1} ,$$

with which the stationary spectral radiance

$$\rho_s \equiv \frac{A}{B} = \frac{8\pi h f_{12}^3}{c^3}$$

can be written. Introducing the general spectral radiance

$$\rho = \varphi h f_{12} / c$$

and requiring  $N = N_1 + N_2$  to be constant for a system of two energy levels, one finds

$$\frac{dN_1}{dt} = \left. \frac{dN_1}{dt} \right|_{\text{ab}} - \left. \frac{dN_2}{dt} \right|_{\text{st}} - \left. \frac{dN_2}{dt} \right|_{\text{sp}} = \rho B (N_2 - N_1) + A N_2 = -\frac{dN_2}{dt} .$$

For  $\Delta N = N_2 - N_1$  then follows that

$$\frac{d\Delta N}{dt} = -2\frac{dN_1}{dt} = -2\rho B\Delta N - 2AN_2 + AN_1 - AN_1 = -2\rho B\Delta N - A\Delta N - AN.$$

After some time an equilibrium is reached inside the active medium, resulting in a vanishing time derivative. In this case, solving for the stationary number difference

$$\Delta N_s = -\frac{AN}{A + 2\rho B} = -\frac{N}{1 + 2\rho/\rho_s}$$

yields  $\Delta N_s < 0$  for any system with only two energy levels.

### 2.3 Necessity of multiple levels

This result directly contradicts the requirement of population inversion  $\Delta N_s > 0$  necessary for the amplification through stimulated emission as discussed previously, preventing the usage of two level systems as the active medium. Adding more energy levels as depicted in Figure 2 solves this problem. Instead of immediately relaxing back to the ground state via spontaneous emission, excited electrons now decay very quickly from  $E_3$  to  $E_2$  and  $E_1$  to  $E_0$  while the  $E_2$  to  $E_1$  transition takes longer. This means that  $A_{21} < A_{32}$  as well as  $A_{21} < A_{10}$  and results in a distribution similar to what is shown below.



**Figure 2:** Exemplary energies and population densities for multiple levels. [1]

One then expects  $N_0, N_2 \gg N_1, N_3$  for  $N \approx N_0 + N_2$  and  $\Delta N \approx N_2$  in the stationary configuration. Accordingly, a population inversion  $\Delta N_s > 0$  is trivial to achieve, making four level systems a suitable choice for laser construction.

Such a system is realized by a He-Ne laser when the red mode at  $\lambda = 633 \text{ nm}$  is used. Table 1 indicates that this corresponds to a transition from the  $3s_2$  to the  $2p_4$  level, on which Figure 3 provides more detailed information.

**Table 1:** Properties for different transitions of the He-Ne laser. [1]

Color	Wavelength (nm)	Transition (Paschen notation)	Output power (mW)	Spectral width (MHz)	Gain (%/m)
<b>Infrared</b>	<b>3391</b>	$3s_2 \rightarrow 3p_4$	>10	280	10,000
Infrared	1523	$2s_2 \rightarrow 2p_1$	1	625	
<b>Infrared</b>	<b>1153</b>	$2s_2 \rightarrow 2p_4$	1	825	
Red	640	$3s_2 \rightarrow 2p_2$			
Red	635	$3s_2 \rightarrow 2p_3$			
<b>Red</b>	<b>633</b>	$3s_2 \rightarrow 2p_4$	>10	1500	10
Red	629	$3s_2 \rightarrow 2p_5$			
Orange	612	$3s_2 \rightarrow 2p_6$	1	1550	1.7
Orange	604	$3s_2 \rightarrow 2p_7$			
Yellow	594	$3s_2 \rightarrow 2p_8$	1	1600	0.5
Green	543	$3s_2 \rightarrow 2p_{10}$	1	1750	0.5

In this setup, the active medium is a mixture of helium and neon gases. Helium atoms are excited to metastable states via electric discharge before colliding with neon atoms to provide excitation and transfer kinetic energy via



The excess energy  $E \simeq 100$  meV is dissipated as heat after the resonant transfer, as it measures about two times the 300 K thermal energy. Due to the selection rules, the upper 2s and 3s levels have lifetimes of the order 100 ns because they can only decay to p levels, while lower states exhibit shorter 10 ns timescales.



**Figure 3:** Energy level diagram of a He-Ne laser in Paschen notation. [1]

## 2.4 Stability for different resonators

To characterize spherical mirrors, the parameter

$$g_k = 1 - \frac{L}{R_k}$$

presents a convenient alternative to the curvature radii. With this, the radius  $w_0$  at the waist of a Gaussian beam as depicted in Figure 4 can be calculated via

$$w_0^4 = \frac{\lambda^2 L^2 g_1 g_2 (1 - g_1 g_2)}{\pi^2 (g_1 + g_2 - 2g_1 g_2)^2}.$$

It is immediately obvious that for  $w_0$  to be a real solution,

$$0 \leq g_1 g_2 \leq 1$$

needs to hold, defining a stability condition for any mode to exist in a given resonator.

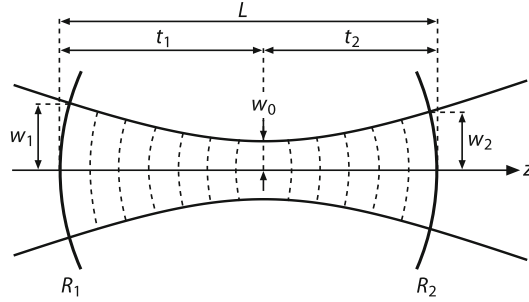


**Figure 4:** Adaptation of a Gaussian beam to a spherical mirror resonator. [1]

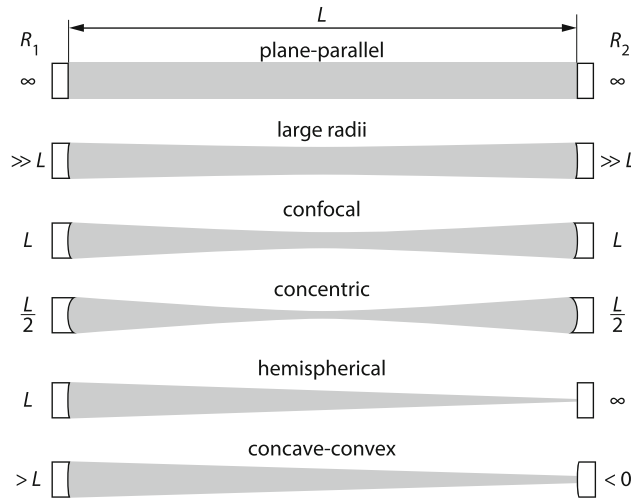


**Figure 5:** Types of stable resonator configurations. [1]



**Table 2:** Available mirrors for the construction of the cavity. [2]

Mirror	Design	Surface
planar	$R_1 = \infty$ flat / flat	HR (high reflectivity) $R \geq 99\%$
concave	$R_1 = 1000$ mm spherical / flat	HR (high reflectivity) $R \geq 99\%$
concave	$R_1 = 1400$ mm spherical / flat	HR (high reflectivity) $R \geq 99\%$
concave	$R_2 = 1400$ mm spherical / flat	OC (out coupling) $T \simeq 2\%$

Figure 5 displays some realizable mirror configurations, while Table 2 lists available parts for the setup at hand. Their stability factors are evaluated graphically in Figure 6 to determine the maximum possible resonator length.

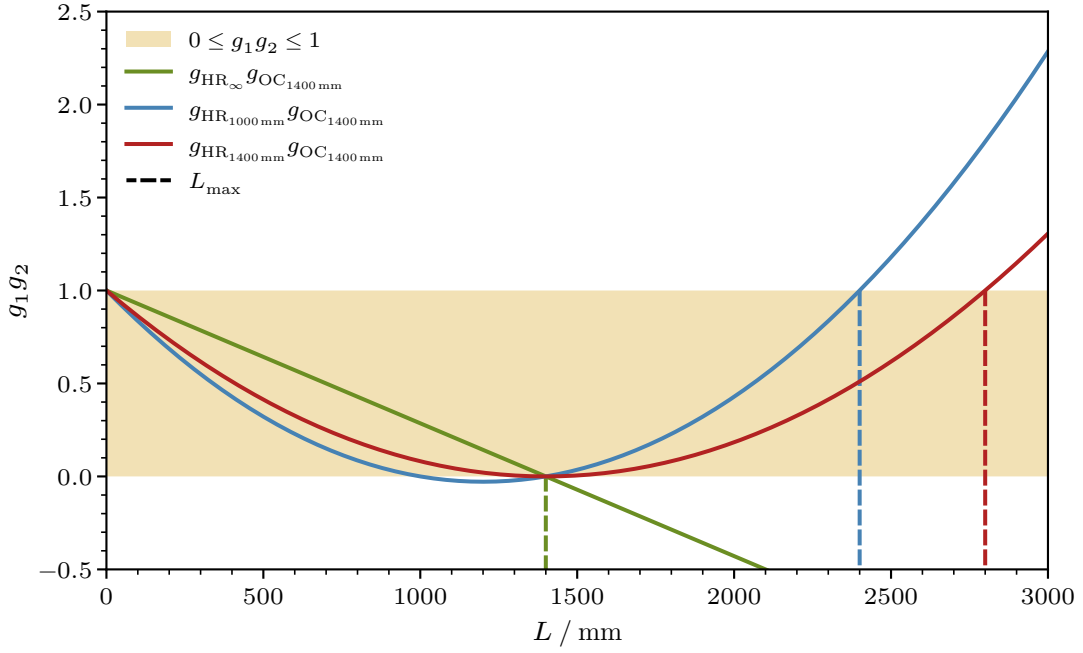


**Figure 6:** Stability diagram as functions of the resonator length.

It should be noted that an unstable resonator with  $g_1g_2 < 0$  or  $g_1g_2 > 1$  does not necessarily preclude laser operation. Unstable lasing implies large diffraction losses, as significant parts of laser power leak around the mirror edges, in turn requiring high optical gain in the active medium to compensate. The resulting configuration can however be less sensitive to disturbances such as thermal lensing or misalignment than a stable resonator, providing desirable properties depending on the application.

## 2.5 Transverse and longitudinal modes

During normal operation, different transverse electromagnetic modes (TEM) interfere in the plane perpendicular to the beam axis. Their orders are denoted using indices like  $\text{TEM}_{r\vartheta}$  and  $\text{TEM}_{xy}$  to give the integer number of nodes in direction of the respective coordinate. Assuming a Gaussian beam profile, circular symmetry can be parametrized by multiplication with Laguerre polynomials. If modes are selected using a thin wire as is the case here, a rectangular symmetry is required. A cut of the electric field strength in  $x$  direction then follows

$$E_n(\xi) = H_n(\xi)e^{-\xi^2/2},$$

where  $H_m(\xi)$  is the appropriate Hermite polynomial and  $\xi = \sqrt{2}x/w_0$  connects the parameter to the spacial coordinate. The first three solutions

$$H_0 = 1, \quad H_1(\xi) = 2\xi, \quad H_2(\xi) = 4\xi^2 - 2$$

lead to the patterns shown in Figure 7 below.

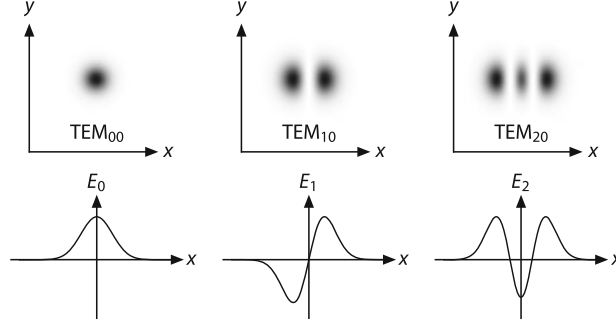


**Figure 7:** Observable  $\text{TEM}_{xy}$  modes for rectangular geometry. [1]

Obtaining the intensity, which is the quantity that is actually measured, requires squaring the absolute value of the electric field amplitude. From  $I \propto |E|^2$  follows

$$I_{\text{TEM}_{00}}(x) = I_{00}e^{-2x^2/w_0^2}, \quad (1)$$

$$I_{\text{TEM}_{10}}(x) = I_{10}x^2e^{-2x^2/w_0^2}/w_0^2, \quad (2)$$

$$I_{\text{TEM}_{20}}(x) = I_{20}(4x^2/w_0^2 - 1)^2e^{-2x^2/w_0^2} \quad (3)$$

as the theoretically expected distributions with arbitrary normalization factors. Additional degrees of freedom may be introduced to account for distortive effects such as a finite background or an asymmetric shape due to inaccurate centering of the probe.

In multimode operation, longitudinal modes in direction of beam expansion instead interfere to produce beating patterns in the signal. This is due to slight frequency variations that result from the multiple allowed standing wave solutions inside the resonator.

## 2.6 Doppler broadening of the transition

This beating pattern is quite complicated, but can be analyzed by decomposing it to its Fourier coefficients. From  $L = m\lambda/2$  for standing waves follows  $f = mc/2L$  or

$$\Delta f_{\text{PP}} = \frac{c}{2L} \quad (4)$$

as the distance between spectral peaks, which is proportional to the reciprocal resonator length with  $\Delta f_{\text{PP}} \simeq 100$  MHz as a typical value. Additionally, the uncertainty principle requires energy levels to have  $\Delta E = h/2\pi\tau$  as a finite width. A natural linewidth

$$\Delta f_{\text{N}} = \frac{1}{2\pi} \left( \frac{1}{\tau_1} + \frac{1}{\tau_2} \right)$$

with lifetimes  $\tau_1$  of the lower and  $\tau_2$  of the upper energy level is the result, which describes a Lorentzian profile

$$F_{\text{N}}(f) = \frac{(\Delta f_{\text{N}}/2)^2}{(f - f_{12})^2 + (\Delta f_{\text{N}}/2)^2}.$$

Values are of the order  $\Delta f_{\text{N}} \simeq 10$  MHz for a He-Ne laser. A homogenous broadening is introduced from elastic collisions, which cause phase shifts during emission. The width

$$\Delta f_{\text{C}} = \sqrt{\frac{3}{4mkT}} d^2 p$$

follows from thermodynamics and has values around  $\Delta f_{\text{C}} \simeq 100$  MHz at temperatures of  $T = 300$  K with the Boltzmann constant  $k$  as well as the mass  $m$  and diameter  $d$  of the atoms. The variable  $p$  denotes the pressure of an ideal gas.

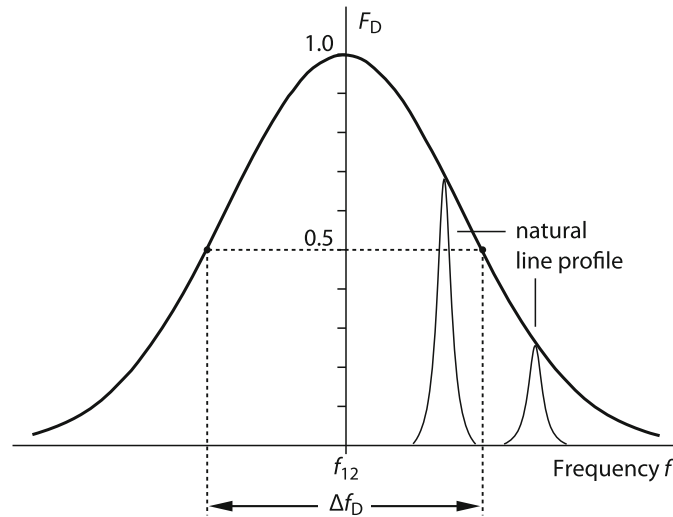


**Figure 8:** Typical Doppler broadening compared to natural line width. [1]

Lastly, the motion of emitting particles inhomogenously shifts the emitted frequency according to the Doppler effect. This can be written for  $v \ll c$  as

$$f'_{12} = f_{12}(1 \pm v/c) ,$$

with the sign indicating movement towards or away from the detector. In case of thermal equilibrium, this obeys Maxwell statistics with a Gaussian line shape function

$$F_D(f) = 2^{-4(f-f_{12})^2/\Delta f_D^2}$$

and a full width half maximum

$$\Delta f_D = 2f_{12}\sqrt{2kT\ln 2/m/c} . \quad (5)$$

Due to values around  $\Delta f_D \simeq 1.5 \text{ GHz}$  for a He-Ne laser, the Gaussian represents an enveloping function with much larger spread than other contributions as can be seen in Figure 8.

## 2.7 Brewster window and polarization

Inserting a Brewster plate at the Brewster angle inside the cavity before the mirror as shown in Figure 9 allows the light component with polarization parallel to the plane of incidence to be transmitted with zero losses due to vanishing reflectivity, while about 20 % of the orthogonally polarized intensity are reflected at each interface and therefore lost. For two passes through two windows, losses accumulate from a total of eight reflections. Due to the nonlinear operation of a laser and by assuming losses per cycle of 2 % at the out coupler as well as a gain around 10 % inside the active medium, one finds that only the parallel part is capable of lasing, making the output fully linearly polarized.

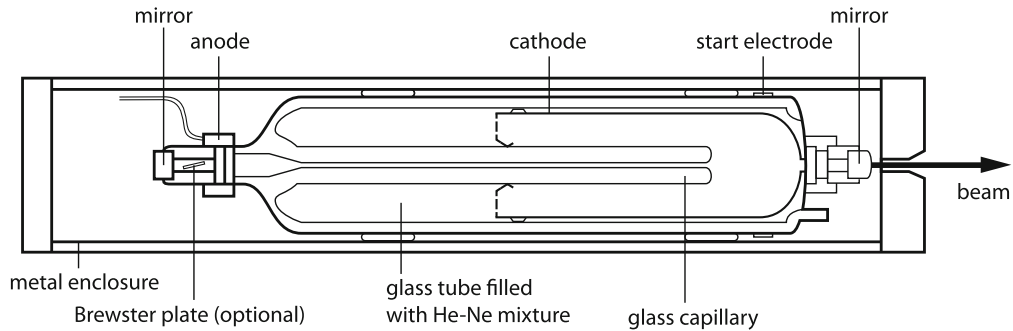


**Figure 9:** Schematic setup of a He-Ne laser generating polarized output. [1]

The intensity of a polarized beam decreases on a perfect polarizer according to Malus

$$I(\theta) = I_0 \cos^2 \theta , \quad (6)$$

with  $\theta$  giving the angle between the initial polarization and the polarizer axis.

## 3 Procedure

### 3.1 Aligning the Laser

The alignment of the He-Ne laser is initiated by positioning an auxiliary alignment laser (wavelength: 532 nm, maximum power: 1 mW, reduced power: 0.2 mW) on the optical bench. A target screen with a cross mark is placed at the end of the optical rail. The alignment laser should be adjusted such that its beam passes through the center of the cross on the target screen. This ensures that the alignment laser coincides with the optical axis of the He-Ne laser.

Next, the He-Ne laser components are positioned in the following order: the laser tube (length: 408 mm, diameter: 1.1 mm), resonator mirrors (diameter: 12.7 mm), and Brewster windows. These components together form the laser resonator, with the Brewster windows ensuring minimal loss while defining the polarization direction. The alignment of these components is critical: the alignment laser's back reflections should be made to hit the target screen's cross at the center, indicating proper alignment along the optical axis.

### 3.2 Verifying the Stability Condition

Once the laser has been aligned, the stability condition must be verified. The laser is adjusted to its maximum power using a photodiode, and the maximum resonator length is set by gradually increasing the gap between the two resonator mirrors. Throughout the process, the laser power is continuously readjusted. With a well-aligned setup, the system should approach the theoretical value from the stability condition. This step is repeated for different resonator lengths to study the effect on the laser's stability.

### 3.3 Observing Transverse Modes

To observe transverse electromagnetic (TEM) modes, a thin tungsten wire (diameter: 0.005 mm) is placed between the resonator mirror and the laser tube. This wire stabilizes different modes, which can be observed on an optical screen. A scattering lens may be used to enlarge the laser beam, making it easier to identify the modes. The wire functions to stabilize the laser beam, enabling clearer mode identification. The optical screen is then replaced with a photodiode to measure the intensity distribution for at least two modes. The measured intensity distributions are plotted and compared with theoretical expectations to validate the mode stability.

### 3.4 Determining the Polarization

The laser's polarization is determined by placing a polarizer behind the outcoupling mirror. The intensity of the laser beam is measured with a photodiode as the polarizer is rotated. The Brewster windows, which minimize reflection losses, ensure a well-defined polarization direction. By comparing the experimental intensity distribution with theoretical calculations, the polarization characteristics of the laser are evaluated, and the influence of the Brewster windows and resonator mirrors on the polarization is examined.

### 3.5 Analyzing Spectra in Multimode Operation

In the absence of a Fabry-Perot etalon, the laser operates in multimode, meaning several longitudinal modes coexist. This leads to temporal intensity variations due to the beating between modes. To analyze these beat frequencies, a fast photodiode with a bandwidth up to 1 GHz is used, and the Fourier spectra are recorded for various resonator lengths with a spectrum analyzer. The spread of the neon transition is compared with the distance between the longitudinal modes, and the multimode operation is justified. Additionally, the dependence of the beat frequency on the resonator length is investigated.

### 3.6 Measuring the Wavelength

The wavelength of the He-Ne laser is determined by using diffraction patterns produced by a slit and diffraction grating. The diffraction maxima and minima are measured to accurately determine the wavelength. This method provides a precise measurement of the laser's wavelength and can be used to verify the laser's output characteristics.

## 4 Results

To analyze the measured data, the Python [3] packages NumPy [4] and SciPy [5] are used, with Matplotlib [6] generating the graphical presentation and Uncertainties [7] allowing for automated linear order propagation of errors.

### 4.1 Verifying the Stability Condition

As shown in Figure 6 the stability condition for the used mirrors is fulfilled for different resonator lengths  $L$ . In the case of one planar mirror ( $R_1 = \infty$ ) and one out coupling mirror with radius  $R_2 = 1400 \text{ nm}$  the stability condition is true for a resonator length of up to 1.4 m. Thus one would expect to see the laser working fine for smaller resonators. Analogously for a high reflective mirror ( $R_1 = 1400 \text{ nm}$ ) instead of the planar surface one

find a maximum length of  $L \leq 2.8$  m. The measured intensities for different resonator

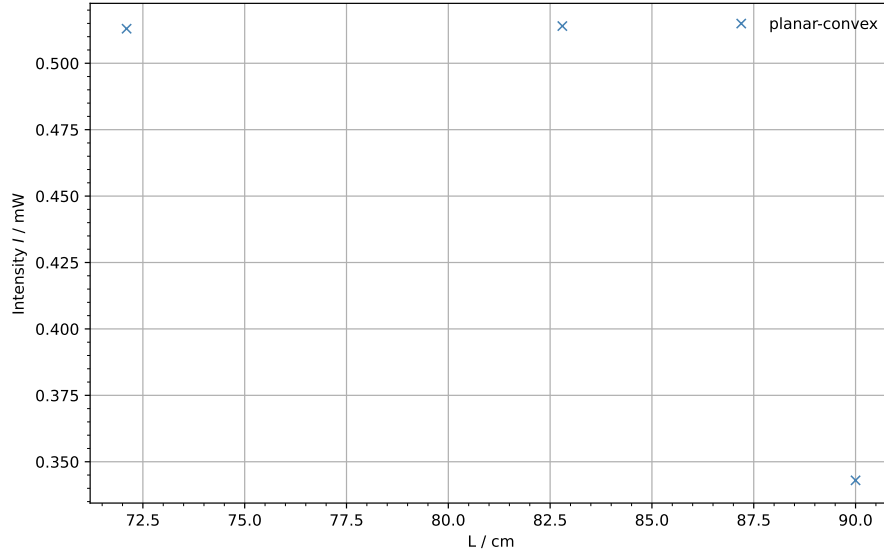


**Figure 10:** Measured Intensity in dependency of resonator length  $L$  to verify the Stability Condition for one planar and one convex mirror.

lengths are displayed in Figure 10 and Figure 11. One can see that the intensities are  $\ll 0$  and therefore a stable operation of the laser is possible.

## 4.2 Observing Transverse Modes

The measured intensities for different deviations of the detector in  $x$  directions are shown in Figure 12, Figure 13 and Figure 14. The respective curve-fits follow the equations shown in (1), (2), (3). Since the measurements are not exactly as predicted, the actual equations need to be adjusted.

### 4.2.1 TEM<sub>00</sub>

For the TEM<sub>00</sub> follows

$$I_{\text{fit,TEM}_{00}}(x) = I_{00} \cdot e^{-\frac{2(x-m)^2}{w_0^2}}.$$

The definition of a new centre of the curve  $m$  is necessary because the detector's deviation scale is not symmetrical around the beam's axis. The parameters for the fit are given

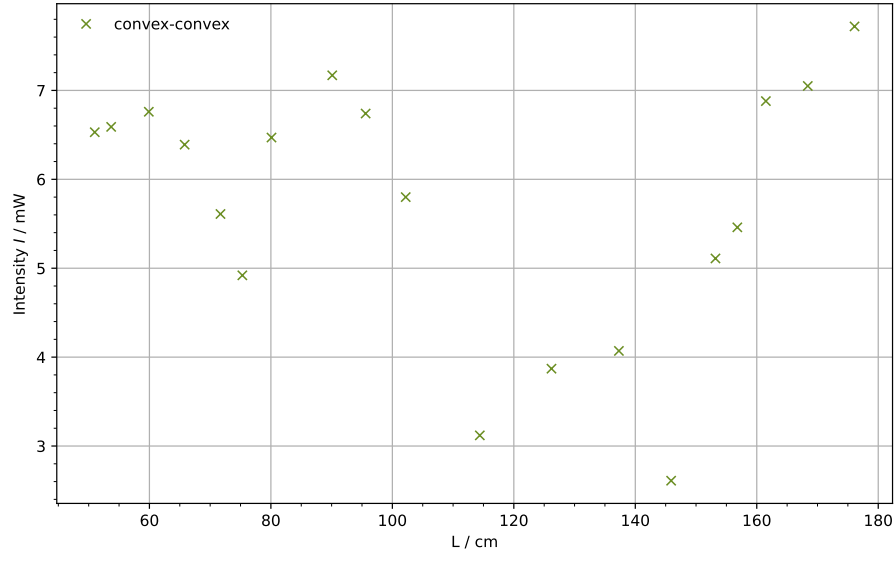


**Figure 11:** Measured Intensity in dependency of resonator length  $L$  to verify the Stability Condition for two convex mirrors.

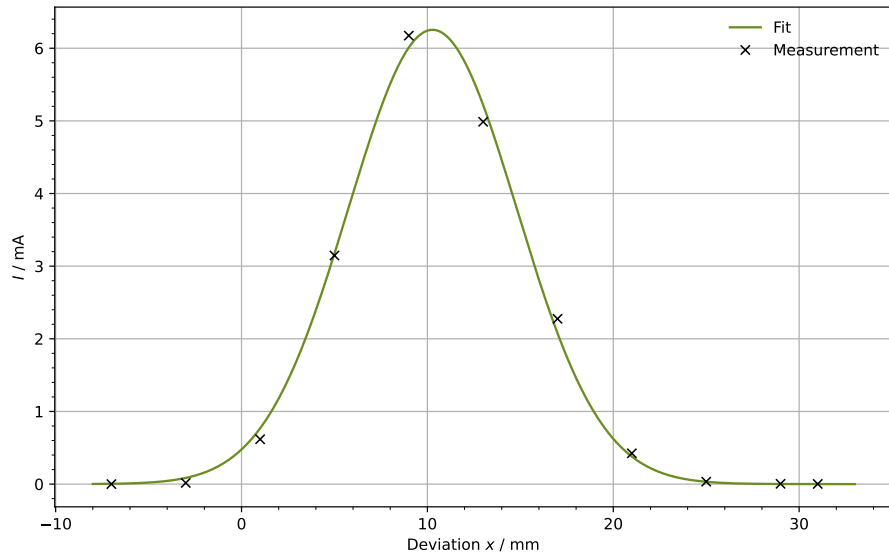


**Figure 12:** Measured Intensity in dependency of the detectors  $x$ -position for observing  $\text{TEM}_{00}$ .



by

$$\begin{aligned} I_{00} &= (6.253 \pm 0.118) \text{ mW} \\ m &= (10.276 \pm 0.099) \text{ mm} \\ w_0 &= (9.058 \pm 0.198) \text{ mm} . \end{aligned}$$

#### 4.2.2 TEM<sub>10</sub>

Analogously to the adjustment for intensity of TEM<sub>00</sub> the new fit curve can be determined to

$$I_{\text{fit,TEM}_{10}}(x) = I_{10} \cdot \left( \frac{x-l}{w_0} \right)^2 \cdot e^{-\frac{2(x-m)^2}{w_0^2}} .$$

The newly introduced parameter  $l$  is needed to describe the asymmetrical properties of the data. For the new defined equation the parameters can be determined to

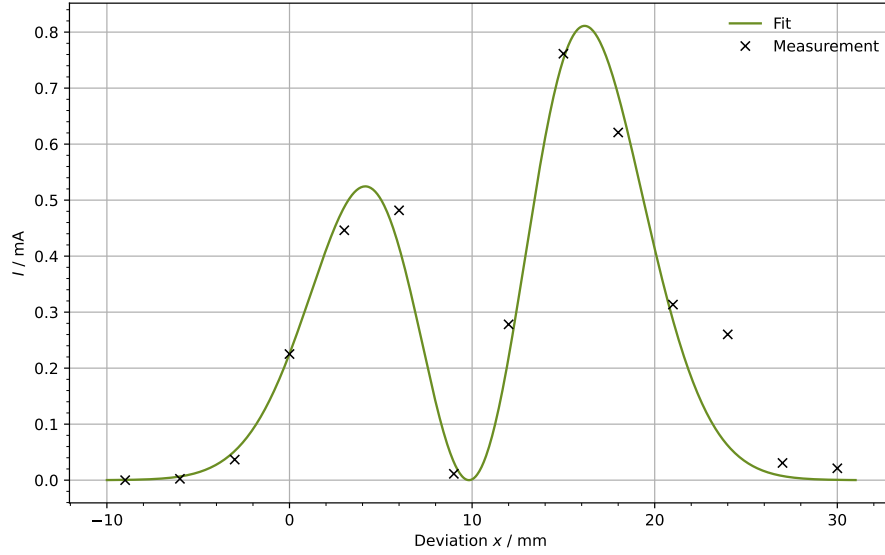


**Figure 13:** Measured Intensity in dependency of the detectors  $x$ -position for observing TEM<sub>10</sub>.

$$\begin{aligned} I_{10} &= (3.568 \pm 0.236) \text{ mW} \\ m &= (10.483 \pm 0.264) \text{ mm} \\ w_0 &= (8.480 \pm 0.335) \text{ mm} \\ l &= (9.830 \pm 0.262) \text{ mm} \end{aligned}$$

### 4.2.3 TEM<sub>20</sub>

The proper fit function can be defined by

$$I_{\text{fit,TEM}_{20}}(x) = I_{20} \cdot \left( 4 \left( \frac{x-l}{w_0} \right)^2 - 1 \right)^2 \cdot e^{-\frac{2(x-m)^2}{w_0^2}} .$$

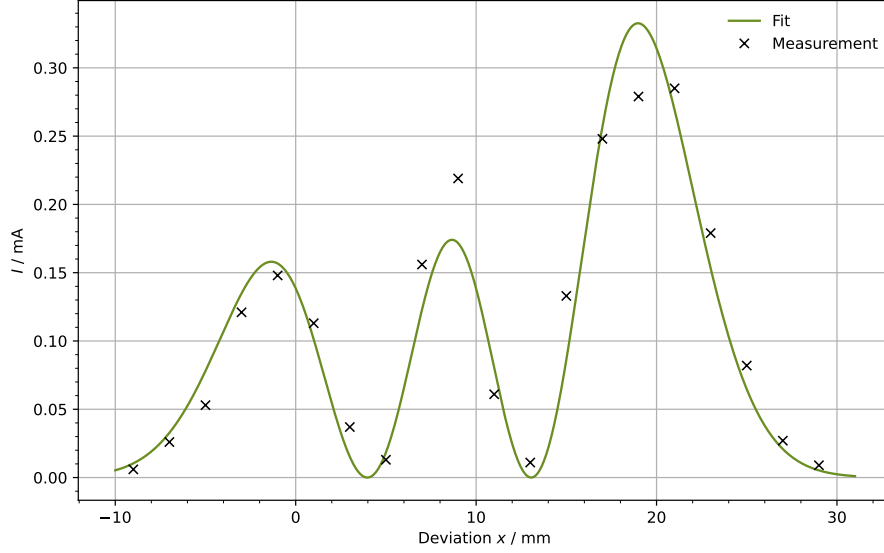


**Figure 14:** Measured Intensity in dependency of the detectors  $x$ -position for observing TEM<sub>20</sub>.

The parameters are

$$I_{20} = (0.176 \pm 0.009) \text{ mW}$$

$$m = (9.266 \pm 0.190) \text{ mm}$$

$$w_0 = (9.082 \pm 0.184) \text{ mm}$$

$$l = (8.511 \pm 0.181) \text{ mm}$$

### 4.3 Determining the Polarization

In order to determine the polarization of the laser, the measured intensities are plotted against the polarization filter's angle. The general dependency of angle and intensity is given via (6). But similar to the chapters above, the equation needs to be slightly adjusted. The final form is

$$I = I_0 \cos(\phi - \alpha)^2 + c .$$

The introduced parameter  $c$  is needed to compensate any offset and  $\alpha$  is used to compensate possible rotation that occurs due to different orientations of the polarization direction. The parameters are

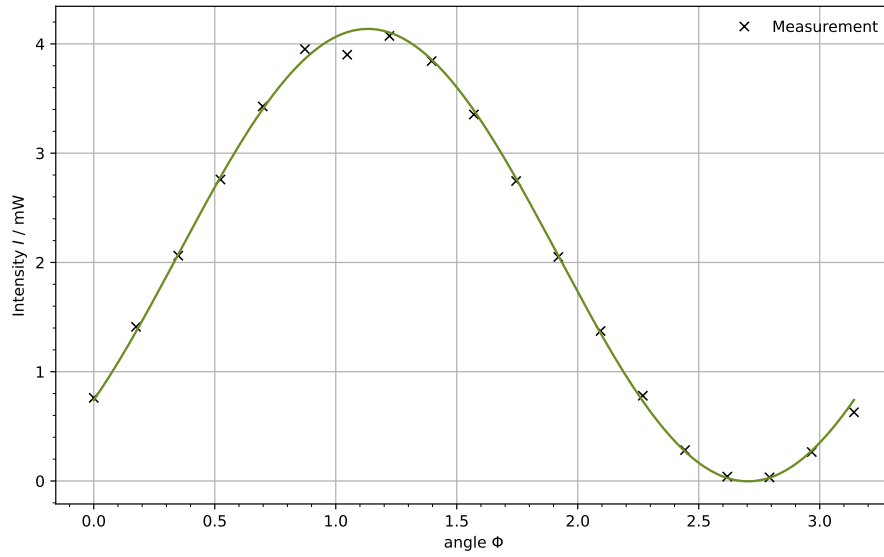


**Figure 15:** Measured Intensity in dependency of the polarization filter's angle.

$$I_0 = (4.140 \pm 0.032) \text{ mW}$$

$$\alpha = 1.133 \pm 0.004$$

$$c = (-0.003 \pm 0.018) \text{ mW} .$$

#### 4.4 Analyzing Spectra in Multimode Operation

The experimental data for frequency and amplitude are shown in Table 3 with the resonator length.

**Table 3:** Experimental data after the FFT.

L in cm	$f_1$ (MHz)	Ampl <sub>1</sub> (mV)	$f_2$ (MHz)	Ampl <sub>2</sub> (mV)	$f_3$ (MHz)	Ampl <sub>3</sub> (mV)	$f_4$ (MHz)	Ampl <sub>4</sub> (mV)	$f_5$ (MHz)	Ampl <sub>5</sub> (mV)
53.7	279	958	560	870	836	740	1117	140	1393	80
65.8	228	988	457	873	682	880	911	480	1141	160
75.3	200	992	398	931	599	830	797	700	994	220
90.1	169	1000	335	950	501	896	667	905	832	800

In order to investigate the dependence of the resonator length and the measured frequencies one needs to calculate the  $\Delta f$  between the peaks.

**Table 4:** Calculated differences between peak frequencies.

L in cm	$\Delta f_{1,2}$ / MHz	$\Delta f_{2,3}$ / MHz	$\Delta f_{3,4}$ / MHz	$\Delta f_{4,5}$ / MHz	avg. $\Delta f$ / MHz
53.7	281.0	276.0	281.0	276.0	278.50
65.8	229.0	225.0	229.0	230.0	228.25
75.3	198.0	201.0	198.0	197.0	198.50
90.1	166.0	166.0	166.0	165.0	165.75

By solving (4) for  $L$  one can obtain the following resonator lengths

$$\Delta f = 278.50 \text{ MHz} \rightarrow 53.8 \text{ cm}$$

$$\Delta f = 228.25 \text{ MHz} \rightarrow 65.7 \text{ cm}$$

$$\Delta f = 198.50 \text{ MHz} \rightarrow 75.6 \text{ cm}$$

$$\Delta f = 165.75 \text{ MHz} \rightarrow 90.5 \text{ cm} .$$

A different approach to clarify the dependence of resonator length and the distance between the spectral peaks is the graphical one shown in Figure 16. The fit for the data is calculated with

$$\Delta f(L) = a \cdot L^b$$

with  $a$  having the theoretical value of  $a = c/2$  and  $b = -1$  as one can obtain from Figure 16. The fit parameters are given by

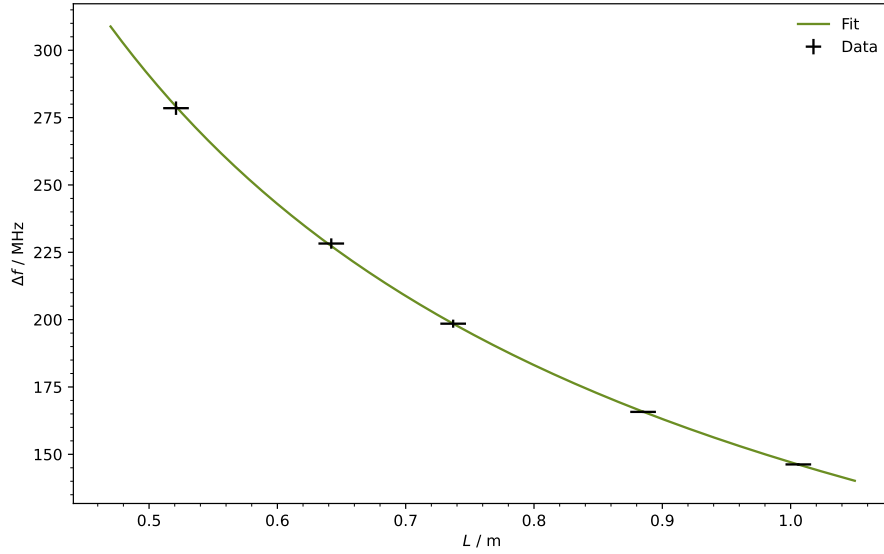


**Figure 16:** Dependence of resonator length and distance between spectral peaks.

$$a = (147.1 \pm 0.1) 10^8 \frac{\text{m}}{\text{s}}$$

$$b = -0.983 \pm 0.004 .$$

Furthermore, an attempt can be made to measure and visualize the Doppler broadening described in subsection 2.6. For doing so, one additional measurement was performed with a larger resonator. Due to the larger resonator, the distance between the spectral peaks decreases and therefore more peaks can be seen, allowing to collect more data. The data are visualized and fitted in Figure 17. The fitted curve follows the form

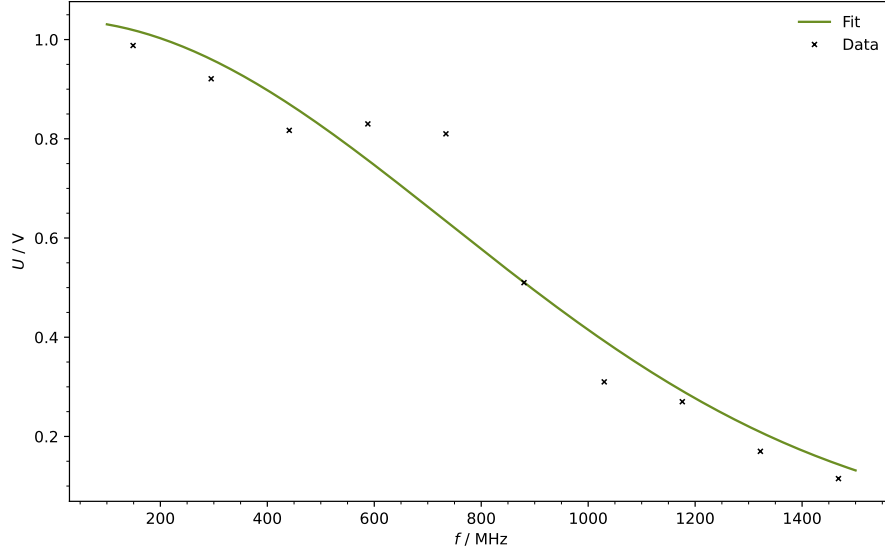


**Figure 17:** Measurement and visualization of Doppler broadening.

$$U(f) = n \cdot \exp \left( -\frac{f^2}{2s^2} \right) .$$

The parameters can be determined to

$$n = (1.04 \pm 0.05) \text{ V}$$

$$s = (738 \pm 43) \text{ MHz} .$$

From here the full width half maximum ( $\Delta f_{\text{D}}$ ) can be calculated using (5)

$$\Delta f_{\text{D}} = (1.7 \pm 0.1) \text{ GHz} .$$

In comparison, the theoretical value mentioned in subsection 2.6 is  $\Delta f_{\text{D}} \approx 1.5 \text{ GHz}$  for a He-Ne laser, while a bandwidth of  $\Delta f_{\text{BW}} = 0.9 \text{ GHz}$  is given for the photodiode.

## 4.5 Measuring the Wavelength

To calculate the wavelength, one finds

$$\lambda = \frac{gx_n}{n\sqrt{d^2 + x_n^2}},$$

with the distance  $x_n$  between the maximum of order  $n$  and the main peak, the slit width  $g$  and the spacing  $d$  of the screen.

**Table 5:** Measured diffraction peak distances on a screen at  $d = (83.2 \pm 1.0)$  cm from different gratings with calculated wavelengths.

$n$	$g = 1/80$ mm		$g = 1/100$ mm	
	$x_{n,\text{left}} / \text{cm}$	$x_{n,\text{right}} / \text{cm}$	$x_{n,\text{left}} / \text{cm}$	$x_{n,\text{right}} / \text{cm}$
1	4.5	4.3	5.4	5.4
2	8.7	8.4	11.1	10.7
3	12.8	12.9	16.5	16.1
4	17.1	17.3	22.2	21.8
5	21.6	22.2		
$\lambda = (641 \pm 10) \text{ nm}$		$\lambda = (644 \pm 9) \text{ nm}$		
$\lambda = (643 \pm 12) \text{ nm}$				

Listed in Table 5 are the measurements with their corresponding results. The derived wavelength  $\lambda = (643 \pm 12)$  nm can be compared to the value  $\lambda = 633$  nm from the literature [1].

## 5 Discussion

Summarizing the obtained results, all theoretical expectations are fulfilled within the given tolerances. Due to limitations in the extend of the setup as well as difficulties in alignment, especially for the plane konvex resonator configuration, the expected intensity drop when reaching the stability limits could not be observed, though the measured lasing range is still in agreement with the allowed  $L$  intervals. The function given by the respective Hermite polynomials and a Gaussian distribution describes the observed TEM profile reasonably well, though measuring steps could have tighter spacing to get a more conclusive picture. The angular dependence of the polarizer fits the theory very well, giving a minimum intensity at  $155^\circ$  compatible with zero, thus confirming the laser beam to be fully polarized thanks to the Brewster window. Similarly, the dependence of frequency maxima position on the reciprocal resonator length can also be verified, while the Doppler broadening seems to represent the dominant influence on the line width. It should be noted, however, that the bandwidth of the photodiode itself leads to a similar

decay and makes this measurement fairly unreliable, likely leading to an underestimation of the effect. Lastly, the wavelength calculated via diffraction maxima agrees with the expected value from the involved transition.

## References

- [1] Hans Joachim Eichler, Jürgen Eichler, and Oliver Lux. *Lasers. Basics, Advances and Applications*. Springer Cham, 2018. ISBN: 978-3-319-99895-4. DOI: <https://doi.org/10.1007/978-3-319-99895-4>.
- [2] *V61, He-Ne laser*. TU Dortmund, Fakultät Physik. 2024.
- [3] *Python*. Version 3.11.0. Oct. 24, 2022. URL: <https://www.python.org>.
- [4] Charles R. Harris et al. “Array programming with NumPy”. In: *Nature* 585.7825 (Sept. 2020), pp. 357–362. DOI: 10.1038/s41586-020-2649-2. URL: <https://doi.org/10.1038/s41586-020-2649-2>.
- [5] Pauli Virtanen et al. “SciPy 1.0: Fundamental Algorithms for Scientific Computing in Python”. Version 1.9.3. In: *Nature Methods* 17 (2020), pp. 261–272. DOI: 10.1038/s41592-019-0686-2.
- [6] John D. Hunter. “Matplotlib: A 2D Graphics Environment”. Version 1.4.3. In: *Computing in Science & Engineering* 9.3 (2007), pp. 90–95. DOI: 10.1109/MCSE.2007.55. URL: <http://matplotlib.org/>. Current version 3.6.2, DOI: 10.5281/zenodo.7275322.
- [7] Eric O. Lebigot. *Uncertainties: a Python package for calculations with uncertainties*. Version 2.4.6.1. URL: <http://pythonhosted.org/uncertainties/>.